CONDENSED-STATE PHYSICS

Synthesis of mesoporous TiO_2 photocatalytically active under visible light or UV radiation

E. A. Ovodok · M. I. Ivanovskaya · S. K. Poznyak · D. A. Kotsikau · S. V. Zlotski · V. V. Uglov · A. E. Seleznev · A. A. Vereschaka

Received: 8 September 2025 / Revised: 20 October 2025 / Accepted: 5 November 2025

Abstract

Mesoporous nanosized titania with a high specific surface area is synthesized by titanium carbide oxidation with nitric acid followed by a heat treatment of the product. The effect of heating temperature on the structural characteristics of TiO_2 and its activity in the photodecomposition reaction of the dye (rhodamine B) is studied. It is shown that compared with the well-known photocatalyst, Degussa P25, the photocatalytic activity of the samples heat-treated at 200°C and 400 °C is improved, when exposed to visible and UV radiation, respectively. The high photoactivity of the TiO_2 sample (200°C) under exposure to visible light is due to a high specific surface area, the presence of CO_x and NO_x groups on the surface, and the structure of the anatase phase with a trace of rutile phase. Under exposure to the UV radiation, the TiO_2 sample (400°C) is characterized by high photoactivity attributed to a high specific surface area and oxygen structure defects (O^-).

Keywords Titania · Photocatalyst · UV Radiation · Visible Light · Structure defects · Rhodamine B

Introduction

One of the problems of the intensively developing world economy is the pollution of the environment, particularly water resources. Synthetic organic compounds and dyes are typical pollutants. Dyes affect the metabolism processes in living organisms; moreover, they can significantly reduce light penetration into the water bodies, thus hindering photosynthesis [1]. Therefore, it is vital to develop effective methods for removing the environmental pollutants. One of the ways is to use the photodecomposition reactions on the surface of the semiconducting materials, such as TiO_2, ZnO, ZrO_2, and SnO_2 [2–6].

The TiO_2-based photocatalysts are of great interest due to their photoactivity, chemical stability, relatively low cost, and nontoxicity [7, 8]. Titania is a semiconductor material with a wide bandgap of about 3.2 eV. In titania, UV radiation generates the electrons and holes reacting with the adsorbed H_2O and O_2 molecules and OH^- ions to form active oxygen species that can interact with organic and inorganic pollutants. Studies aimed at expanding the absorbance spectrum of TiO_2 in the visible region should be carried out to improve the titania photocatalytic activity. One approach to redshift the absorption edge is doping of TiO_2-based materials with nonmetals and transition metal ions [9–13]. Another approach to using visible light in the photocatalytic degradation of organic dyes is to sensitize the catalysts with dyes. The dye-sensitized photocatalysts absorb visible light, followed by a transfer of the excited electrons from the lowest occupied molecular orbital (LUMO) of the dye to the TiO_2 conduction band. Further, in the conduction band, the electrons react with the adsorbed oxygen, generating active oxygen species that destroy the organic pollutants. Generally, for research purposes

https://doi.org/10.1007/s11182-025-03621-x

the dye solutions based on rhodamine, methyl orange, methylene blue, etc. are used in model systems [11, 12, 14].

Their small specific area, low surface adsorption capacity, particle aggregation tendency, and low solar adsorption often limit the photocatalytic efficiency of TiO_2 particles [7, 8]. A more effective solar radiation conversion requires photoactive titania with a developed surface and a high porosity, which is typical for mesoporous nanocrystalline particles. The synthesis of mesoporous titania with crystalline pore walls is a rather difficult task, as during the heat treatment, the amorphous phase transforms into a crystalline one, and the pores collapse. In some cases, organic templates are used to organize the mesoporous structure [15, 16]. However, their use does not allow synthesizing TiO_2 samples at relatively low heating temperatures. One of the well-known template-free methods for synthesizing mesoporous TiO_2 is the oxidation of titanium carbide with nitric acid [17, 18]. In the earlier studies [19, 20], we optimized the parameters of this method by varying the oxidation and heating conditions.

This work aims to establish the structural factors responsible for the photocatalytic activity of the nanosized titanium dioxide with a high specific surface area and a mesoporous structure synthesized by the oxidation of titanium carbide with nitric acid followed by its heat treatment.

Experimental

Synthesis

Mesoporous TiO_2 powder samples were formed by the oxidation of titanium carbide TiC (99.5% metal base) with nitric acid according to the method described before [18, 19]. In this work, however, the nitric acid concentration and the component ratios were changed to provide a proper control over the oxidation process. The synthesis was carried out in a water bath at 70 °C. After the acid was added to the titanium carbide, the resulting suspension was stirred for 1 h. A change of the suspension color from black to yellow indicates that the following transformation $TiC \rightarrow TiO(NO_3)_2 \rightarrow TiO_2 \cdot nH_2O$ is taking place. The complex mechanism of the autocatalytic oxidation of TiC in the presence of NO_2 is described elsewhere [19]. The initial transformation process can be presented as follows:

$$TiC + 4HNO_3 \rightarrow TiO(NO_3)_2 + 2NO_2 + CO + 2H_2O, \quad (1)$$

$$TiO(NO_3)_2 + (n+1)H_2O \rightarrow TiO_2\, nH_2O + 2HNO_3. \quad (2)$$

The resulting $TiO_2 \cdot n$H2O precipitate was filtered and then washed three times in ethanol. The product was dried at 70 °C (sample T-70) and then heated at 200 °C (sample T-200) and 400 °C (sample T-400) in the air at a temperature rise rate of 10 °C/min for 1 h. The prepared powdered samples were further studied using various methods.

Characterization

The samples were characterized by the X-ray diffraction (XRD) analysis, scanning (SEM) and transmission (TEM) electron microscopy, Fourier-transformed infrared (IR) and Raman spectroscopy, X-ray photoelectron spectroscopy (XPS), and electron paramagnetic resonance (EPR). The differential scanning calorimetry (DSC) of the T-70 sample was carried out using a NETZSCH STA 449 C thermal analyser at 20–800°C at the rate of temperature rise of 10 °C/min in a standard air atmosphere.

The XRD measurements were carried out using a Philips X-ray PANalytical Empyrean diffractometer with CuKα radiation at 0.4 deg/min. The size of the coherent scattering regions (CSR) was computed by the Debye-Scherrer equation

$$D = 0.9\lambda / k cos\theta,$$

where k is the full width at half maximum (FWHM) of the peak, θ is the diffraction angle, and λ is the X-ray radiation wavelength.

The porosity (calculated by the Barrett-Joyner-Halend (BJH) method) and the surface area (calculated by the Brunauer-Emmett-Teller (BET) method) were estimated from nitrogen adsorption at 77 K on a Micromeritics ASAP2020 instrument. The size and morphology of the TiO_2 particles were characterized by SEM and TEM using the LEO 1420 and LEO-906E microscopes, respectively.

The IR spectra were recorded on an AVATAR-330 Thermo Nicolet FT-IR spectrometer equipped with a Smart Diffuse Reflectance accessory in the wavelength range of 400–4000 cm^{-1}. The Raman spectra were recorded using a Bruker Senterra dispersive microscope, $\lambda_{ex} = 785$ nm.

The EPR spectra were recorded at 77 and 298 K on a VARIAN E 112 spectrometer at 9.35 GHz (X-range). The microwave radiation power was 5 mW and the modulation amplitude was 0.1 mT at a modulation frequency of 25 kHz. The g-factors and the concentration of paramagnetic centers (PCs) were determined relative to the reference samples: the g-factor relative to the position of the lines of the hyperfine structure (HFS) of Mn^{2+}/MgO and the concentration of PCs relative to a carbon standard.

The X-ray photoelectron spectroscopy (XPS) examination was carried out using a Kratos DLD Ultra spectrometer with an AlK_α X-ray source (monochromator) operated at 225 W. A pass-energy (PE) of 160 eV was used for the survey spectra, and, for the region scans, the PE was 40 eV. The spectra were calibrated to 530.1 eV, binding energy (BE) of the O1s signal, and to 284.8 eV, BE of the C1s signal. The charge neutralization was necessary for all samples. For the deconvolution of the region files, a background subtraction (linear for O1s and C1s, Shirley for Ti2p) was performed before the calculation. The data evaluation was carried out with the CasaXPS software version 2.3.17.

The photocatalytic activity of the samples T-200 and T-400 and the commercially produced Degussa P25 (for comparison) was evaluated in the model reactions of dye bleaching, rhodamine B, under visible light and UV irradiation. The powder in the amount of 80 μg was added to 80 mL of a 0.02 mM rhodamine B solution. The Philips Accentline Halogen (12 V, 30 W) lamp with a UV light filter that cuts off the radiation with wavelengths less than 400 nm was used for the visible light irradiation. A NARVA UVK-125 mercury lamp 2 was used to generate the UV irradiation. The changes in the rhodamine B concentration were detected by a SHIMADZU UV-2550 UV-Vis spectrophotometer.

Results and discussion

Structure of the samples

The results of the structural-phase study, the measurements of the particle size, specific surface area (S), porosity (pore diameter (d_{pore}) and pore volume (V_{pore})) under different heating conditions are shown in Table 1. The prepared TiO_2 samples are nanocrystalline and are characterized by a mesoporous structure and a high specific surface area. The sample heated at 200 °C (T-200) has the highest specific surface area.

All samples possess the anatase crystalline phase with the unit cell parameters corresponding to the reference data (JCPDS Nos. 88-1175 and 84-1286). According to the XRD data, the TiO_2 particles with the anatase crystalline phase were formed as early as at 70 °C in the oxidation process by nitric acid. However, a significant broadening of the reflections in the diffraction patterns suggests the presence of an amorphous phase remaining

Table 1 Phase composition, Particle size, Specific surface area, and Porosity of TiO_2 Samples

T, °C (atmosphere)	Sample	Phase composition	d_{CSR}, nm	*S*, $m^2\ g^{-1}$	D_{pore}, nm	V_{pore}, $cm^3\ g^{-1}$
–	T-70	Anatase+amorphous	4.0	290	3.1	0.224
200 (air)	T-200	Anatase +amorphous	3.9	353	3.4	0.300
400 (air)	T-400	Anatase	7.4	135	5.5	0.185
Degussa P25	–	Anatase +rutile	21	35–65	–	

Fig. 1 XRD patterns of TiO_2 samples heat treated under different conditions

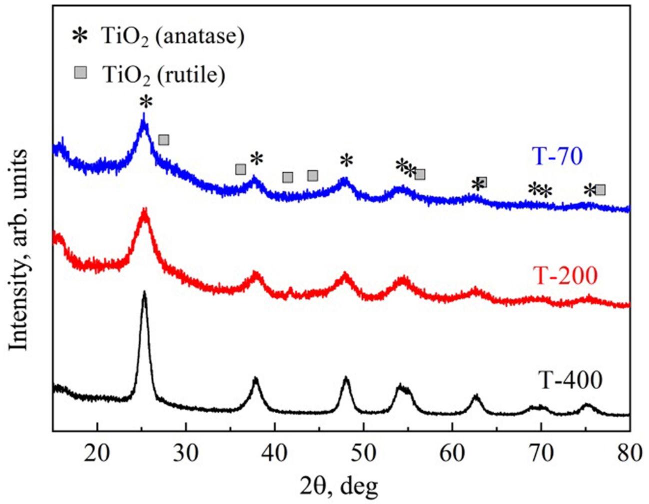

in the samples even after the heating at 200 °C (Fig. 1). The halo extends to the peak region of the rutile phase, suggesting the presence of a [TiO_6] coordination characteristic of the rutile phase.

It is well known [21] that the nitrate-nitrite groups in hydrated metal oxides can slow the oxide crystallization and particle growth to the temperatures of about 500 °C. However, in our samples, no amorphous phase is detected after heating at 400 °C, the particle size almost doubles, and the specific surface area significantly decreases (by about 2.5 times) (see Table 1). The pore diameter and volume also change.

According to TEM, the particles in sample T-200 are round with a size of about 4 nm, which is close to or less than d_{CSR} (Fig. 2a). In the T-400 sample, the particles with $d = 7–9$ nm predominate (Fig. 2b), which, taking into account their polydispersity, is consistent with the value of $d_{CSR} = 7.4$ nm.

Fig. 2 TEM images of TiO_2 powders heat treated at 200 °C T-200 (**a**) and 400 °C T-400 (**b**)

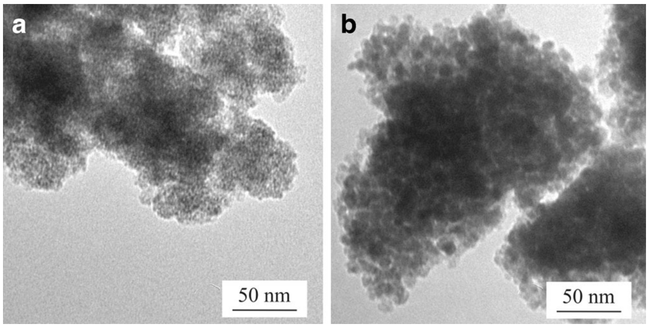

Fig. 3 TG/DSC curves of TiO_2 powder (T-70) prepared by oxidation of TiC with nitric acid and dried at 70 °C

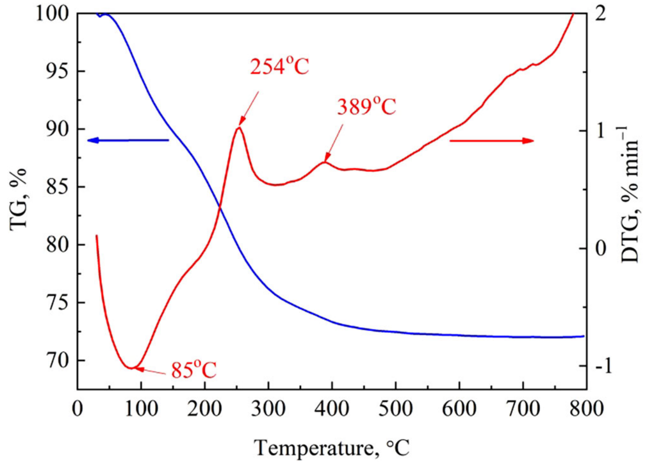

Thermal analysis

Using the TG/DSC curves (Fig. 3), one can describe the transformations occurring during heating of the product of the chemical oxidation of TiC by nitric acid. The low-temperature endothermal effect with a peak at 85 °C, accompanied by a weight loss of 11%, may be due to the removal of weakly bound water and nitrates. Their removal releases the pores, which increases the specific surface area. As mentioned above, the particle size and crystallinity did not change up to 200 °C. The amorphous phase remains in the product, consistent with the DSC data in this temperature range. Above 200 °C, the exothermal effect starts and reaches its maximum at 254 °C. In this case, there is a significant loss of mass (about 15%) and heat release. It is the processes of carbon oxidation ($C \rightarrow CO \rightarrow CO_2$) and TiO_2 crystallization which mainly contribute to this effect. Above 300 °C, the mass loss slows down. A small exothermal effect with a maximum at 389 °C may reflect a further oxidation of the carbon-containing impurities and an improvement of the oxide crystal structure, which is confirmed by the X-ray diffraction patterns—the reflections of the anatase phase become narrower (Fig. 1).

IR and raman spectroscopy

Considering the computed data on the activity of certain Ti-O vibrations in the spectra, we analysed the IR and Raman spectra in these characteristic ranges. As our samples contain the anatase phase, one would expect four

Fig. 4 IR spectra (**a**) and fragments of IR spectra (**b**) of TiO_2 powders heat treated under different conditions

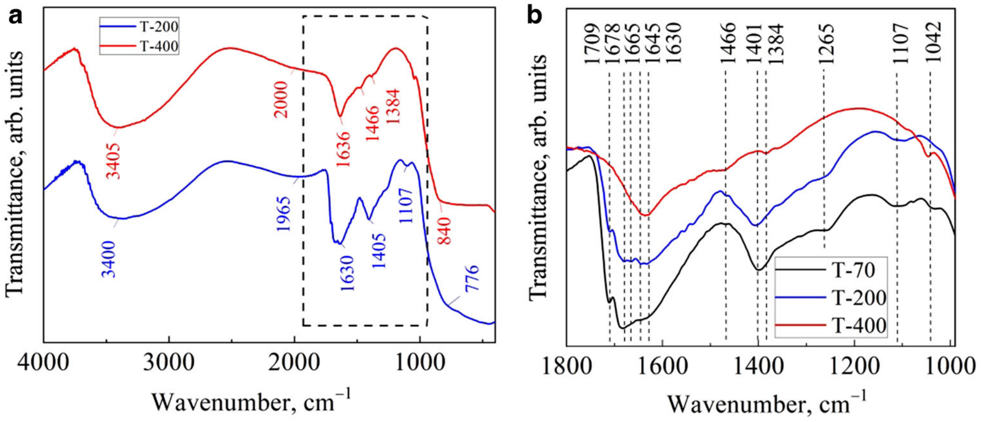

active vibrations (A_{2u} + $3E_u$) in the IR spectra and six vibrations (A_{1g} + $2B_{1g}$ + $3E_g$) in the Raman spectra [22, 23].

A diffuse absorption band is observed in the IR spectra in the 400–850 cm^{-1} range (Fig. 4a). It is a superposition of several normal vibrations ν(Ti-O) characteristic of titanium dioxide in the nanodispersed and insufficiently crystallized samples. The observed band position shift from 776 to 840 cm^{-1} with an increase in the heating temperature of TiO_2 indicates an improvement in the anatase crystal structure [22].

It is necessary to study the IR spectra in the wavenumber range of 1000–1800 cm^{-1} to establish the chemical state of N- and C-containing impurities [23–25]. Figure 4b shows the fragments of IR spectra. The complexity of the analysis lies in the fact that the vibrations of hydroxyl, nitrate-nitrite, and carbonate-carboxylate groups overlap in this spectral um region [26]. When analyzing the spectrum, one should consider that in different heat-treatment stages, the content of NO_2 and CO and the form of their binding with the main synthesis product will differ. Thus, the NO_x-containing groups are less thermally stable than the CO_x-containing ones. At low temperatures, the nitrate ions are stable. However, they transform into radical forms, NO_x, as the temperature rises. Therefore, in the IR spectrum of sample T-200, the N-O bond vibrations quantitively predominate, and in the case of T-400, the C-O vibrations prevail. In the IR spectrum fragments in the wavenumber range of 1000–1800 cm^{-1} (See Fig. 4b), one can notice that at 400 °C, the lines corresponding to the NOx-containing groups (1042, 1107, 1265, 1401, 1678, and 1709 cm^{-1}) disappear, while the low-intensity lines corresponding to the stretch vibrations in COO^- ions (1384 and 1466 cm^{-1}) remain [25].

According to the IR spectrum of the T-200 sample, it contains the ions of different types of the NO_x coordination groups. Titanium atoms can coordinate NO_3^- ions via one or two oxygen atoms ($Ti - O - N \ll^{O}_{O}$ and $Ti <^{O}_{O}> N = O$), and they can also form bridge bonds ($^{Ti-O}_{Ti-O} > N = O$) [26, 27]. The NO_2^- group can be bound with titanium in two ways: $Ti - N \ll^{O}_{O}$ or Ti–O–N=O. It is necessary to analyze the IR spectrum in the wavenumber range of 1644–1710 cm^{-1} to establish the coordination type of nitrate groups [23, 24]. In the case of the T-200 sample, one can observe four absorption lines in this region (1645, 1665, 1678, and 1709 cm^{-1}), which is characteristic of the presence of two types of coordination: bi- and monodentate. Recall that nitrate-nitrite groups of different coordinations in the sample preserve oxide disorder and prevent titania sintering.

The broad band at 1900 cm^{-1} due to the CO stretch vibrations in the spectrum of the T-200 sample can be caused by the CO complexes adsorbed on TiO_2. At low temperatures, an incomplete carbon oxidation takes place to form CO. At 400 °C, the intensity of this band decreases, shifting towards higher frequencies (2000 cm^{-1}). This effect could be accounted for by a change in the adsorption form of CO [23, 25]. The νCO frequency is a measure of the CO-metal bond strength; the observed increase in the vibration frequency ν(CO) is a consequence of the transition from the bridge adsorption $^{Ti}_{Ti}> C = O$ (1900 cm^{-1}) to a linear adsorption form Ti-CO (2000 cm^{-1}).

The intensive absorption bands due to the δ(H-O-H) deformation at 1629–1636 cm^{-1} and the stretching asymmetric ν_{as}(O-H) vibrations (a broad band at 3200–3370 cm^{-1}) in H_2O molecules confirm the presence of water and hydroxyl groups I in the samples (Fig. 4). There are no significant differences in the spectra of samples T-200 and T-400.

Figure 5 shows the Raman spectra. The positions of the vibration lines of Ti-O bonds are listed in Table 2. Five lines, typical for the TiO_2 with an anatase structure, are registered in the range of the normal Ti-O vibrations. A shifting of the intense and narrow line $E_{g(1)}$ towards higher frequencies is typical for nanodispersed samples. The E_g vibration at 144 cm^{-1} is of a bending type. An increase in the frequency of this band is usually attributed to the decreasing particle size and the nonstoichiometric nature of TiO_2 samples caused by a deficit of oxygen in the crystal lattice. The observed frequency of this vibration in the spectra of samples T-200 and T-400 correlates with the titanium dioxide particle size.

Lines G and D, attributed to the condensed forms of carbon, are not registered in the Raman spectra. Low temperatures and an oxidizing environment during the synthesis do not favor the formation of condensed carbon forms [28].

Fig. 5 Raman spectra of TiO_2 samples heat treated under different conditions

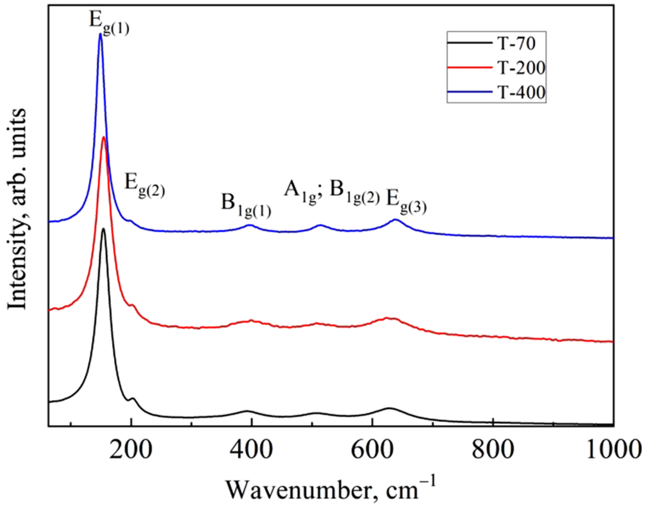

Electronic paramagnetic resonance

As can be seen in Fig. 6, an EPR signal with the central line at $g = 2.002$, half-width (FWHM) $\Delta B = 0.5$ mT, and weakly pronounced side, broadened lines, is observed in the spectrum of sample T-200. The spectrum of such a shape can be considered as two signals of a triplet form with the central line at $g = g_e$ and a double set of HFSs. Signals of this type can be attributed to the N-containing radicals with one unpaired electron ($s = 1/2$) and an HFS from 14 N (nuclear spin $I = 1$, number of lines in the spectrum $n = 2I + 1$, 14 N content 99.635%) [29–31]. One of the HFS constants is ${}^{N}A_1 = 2.5 \pm 0.1$ mT, and the other one (more intensive) is ${}^{N}A_2 = 5.6 \pm 0.1$ mT. Considering the hyperfine lines, the total concentration of PCs is $4{\cdot}10^{16}$ spin g^{-1}.

A similar signal, but half as intense, was observed in the spectrum of sample T-400. The signal also has a double set of HFS components but with less splitting: ${}^{N}A_1 = 1.6 \pm 0.1$ mT, ${}^{N}A_2 = 3.7 \pm 0.1$ mT.

It is known that NO_2^- and NO_3^- ions are not paramagnetic, while the following species are: NO_2^{2-}, NO_2, NO^{2-}, NO, and N. In the EPR spectra of PCs containing one unpaired electron ($s = 1/2$) and one ^{14}N atom with the nuclear spin $I = 1$ (^{14}N), the signal from three lines of approximately equal intensity would be observed at a distance equal to the value of splitting of the hyperfine interaction ${}^{N}A$.

The value of the hyperfine interaction of the electron spin with the nuclear spin, ${}^{N}A$, depends on the delocalization degree of the unpaired electron density on the nitrogen nucleus [29–31]. This parameter is the most

Fig. 6 EPR spectrum of sample T-200 recorded at 298 K

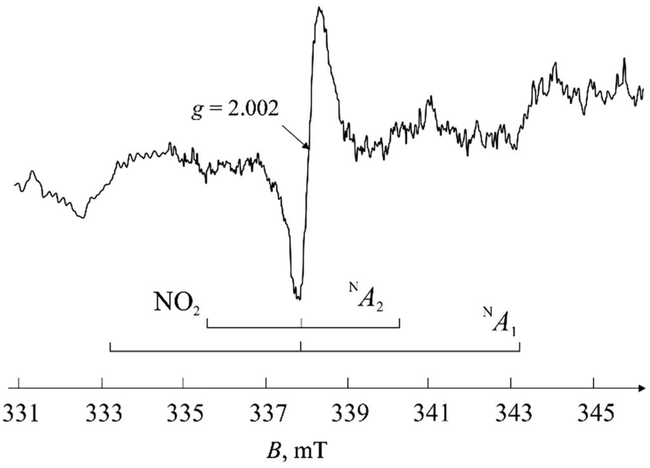

Table 2 Basic Ti-O Vibrations (cm^{-1}) in Raman Spectra of Samples Heat Treated under Different Conditions

Sample	Oscillation type					Phase composition	CSR, nm
	$E_{g(1)}$ O-Ti-O	$E_{g(2)}$ O-Ti-O	$B_{1g(1)}$ Ti-O	A_{1g}; $B_{1g(2)}$ Ti-O	$E_{g(3)}$ O-Ti-O		
T-70	154.1	202.4*	391.7	506.6	628.1	Anatase + amorphous	4.0
T-200	154.6	201.8*	399.3	507.5	623.3	Anatase + amorphous	3.9
T-400	149.1	200.0*	395.9	514.1	637.1	Anatase	7.4
Computation	144	197	399	507, 519	639	Monocrystal anatase	

*Very weak lines

important for determining the nature of PC NO_x from the EPR spectra. Among the radicals and ion-radical of NO_x-type described in the literature, a large value of $^{N}A = 5.6 \pm 0.1$ mT is typical only for condensed radicals $^{\cdot}NO_2$. Only this radical has a strong interaction of the unpaired electron with the magnetic momentum of the ^{14}N atomic nucleus, since the electron predominantly occupies the 2s orbital of nitrogen, and the 2p/2s ratio is small. Radical $^{\cdot}NO_2$ is the main intermediate product of nitrate decomposition, and its formation and stabilization in the TiO_2 are quite expected under the experimental conditions. The $^{\cdot}NO_2$ stabilization was observed in insufficiently crystalized metal oxides (Al_2O_3, TiO_2, ZnO, and SnO_2) during the thermal decomposition of nitrates or hydroxides with NO_3^- and NH_4OH additives [21, 32–34]. Nitrogen-containing radicals preserve the disordered structure of the oxide and hinder its crystallization upon heating.

Two types of $^{\cdot}NO_2$ radicals differentiating in ^{N}A value are due to two forms of their orientation on the titanium dioxide (linear and angle adsorption) [19, 35]. Their occurrence is a consequence of different types of coordination of NO_3^- ions on the T-200 sample, which follows from the IR spectroscopy data (Fig. 4).

In the case of sample T-400, the lower value of ^{14}N hyperfine splitting constant ($^{N}A = 3.7$ mT) can be explained by a stronger electron interaction of NO_2 with the oxide, accompanied by a shift of the unpaired electron density from ^{14}N nucleus to d orbital of Ti^{4+} ion. Apparently, above 400 °C, there remain only strongly adsorbed $^{\cdot}NO_2$ radicals. The ^{N}A value of 1.6 mT is typical for NO_2^{2-} ion-radicals in TiO_2 [30]. In sample T-400, the formation of such radicals is possible during the thermal decomposition of nitrate ions and NO adsorption on oxygen ions, O^{2-}, in the TiO_2 cell

$$O^{2-}_{cell} + NO_g \rightarrow NO^{2-}_{2\ surface}. \tag{3}$$

If the recording temperature of the EPR spectra decreases from 298 to 77 K, the signal intensity increases in sample T-200. However, the spectrum of sample T-400 changes in a more complex fashion, with new signals appearing (Fig. 7). The central line in the spectrum of sample T-400 is three times stronger than the weak lines of the HFS. These changes may be due to the appearance of new resonance lines in the $g = g_e$ region, which do not have HFS lines from ^{14}N and are not detected at 298 K. Moreover, new signals appear at 2.009 and 1.94.

The spectrum was divided into component signals, taking into account the oxidizing conditions of TiO_2 formation, the theoretical ideas about the structure of the centers, O^-, O_2^-, O_3^-, and NO_x, and the calculated parameters of their EPR spectra [29–31, 36], as well as numerous experimental studies [29–40]. The signals related to different nitrogen-containing paramagnetic centers have been identified: $g = 2.002$, $^{N}A = 3.7$ mT; radical $^{\cdot}NO$ – $g_{\perp} = 2.001$, $^{N}A_{\perp} = 1.5$ mT, $g_{II} = 1.94$ [29–35]. In mesoporous titania, the $^{\cdot}NO$ radical can be stabilized in pores [33]; however, in condensed materials, it is unstable, and NO_2^{2-} is formed via reaction (3).

One of the most pronounced changes is the appearance of a new, most intense signal of an axial shape with $g_{II} = 2.009$, $g = 2.002$ in the EPR spectrum of sample T-400 at 77 K. Due to its shape and g-tensor value, this signal can be attributed to the O_3^- species [33, 36–40]. They arise during the adsorption of molecular oxygen on the O^- center [38–40], which possesses high activity at room temperature and can be generated on certain oxides. Center O^- is the surface center that forms in the anion position in the first surface oxide layer: $(O^-)_s^+$.

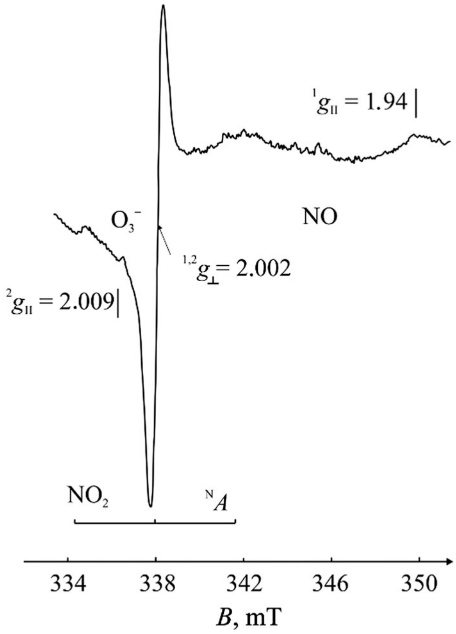

Fig. 7 EPR spectrum of sample T-400 recorded at 77 K

The mechanism of its formation and properties were most fully studied in the non-conducting oxide MgO [38–40]. Due to high activity and fast electron exchange between the centers in conducting oxides, the ^{17}O fine structure lines are poorly resolved, making it difficult to study them [35, 36].

Different mechanisms of O^- center formation are known in oxides. During the TiO_2 synthesis in an oxidizing atmosphere and heating at 400 °C, they can arise due to the following:

- from terminal hydroxyl groups during thermal degradation and O-H bond cleavage:

$$OH^- \ldots {}^- HO \rightarrow O^- + H_2O + e^-; \tag{4}$$

- during the thermal decomposition of nitrates:

$$NO_3^- \rightarrow N_2O \rightarrow O^- + N_2; \tag{5}$$

- from the hydroxyl groups and adsorbed oxygen forms:

$$OH^- + O_2^- \rightarrow O^- + {}^- OOH; \tag{6}$$

- from oxygen ions of the lattice near the cation vacancy (V_k):

$$[V_k - O^-] or [O^- - V_k - O^-]. \tag{7}$$

Above 400 °C, most nitrogen-containing products are removed; the maximum yield of nitrogen occurs during the decomposition of nitrogen oxides at 210–270 °C. The signals from $^{\cdot}NO_2$ and NO radicals are weak in spectra of T-400, but the signal from O_3^- anion-radicals, resulting from O^- formation and adsorption of O_2 on them, appears to be of higher intensity. These results suggest that the formation of O^- in the T-400 sample occurs mainly via reaction (5).

It is only oxygen adsorption which makes it possible to record the O^- center resonance in the EPR spectra, and the interaction with CO also stabilizes this center on TiO_2 [37]. It was noted by a number of authors [37–40] that the signal from O_3^- centers can be detected in EPR spectra only at low temperatures. The signal was identified using *g* factor values and ^{17}O hyperfine splitting constants, its peroxy-type (O^{-}_{cell}-O-O) was grounded, and the schemes of its formation on the MgO surface were suggested [40]. Similarly, O_3^- centers can also be stabilized on other oxides. According to Mikheikin et al. [41], the parameters of the EPR signal from O_3^- centers on different materials, including TiO_2 and SiO_2, are the following: $g_{II} = 2.008$, $g_{\perp} = 2.001$. Peroxide radicals O_3^- on TiO_2 have a *g*-tensor of $g_{II} = 2.0062$, $g_{\perp} = 2.0025$ [33]. Figure 8 shows the formation scheme of the O_3^-paramagnetic center on the titanium dioxide surface.

X-ray photoemission spectroscopy

Table 3 presents the XPS spectra of the T-200 and T-400 samples. The Ti 2p and O 1s spectra are typical for polycrystalline titania [42]. The Ti $2p_{3/2}$ peak in the spectrum of sample T-200 is wider than that in the spectrum of sample T-400 due to the imperfection of the TiO_2 crystal structure and surface inhomogeneity because of the presence of OH, NO_x, and CO_x species after heating at 200 °C.

The O 1s spectra show two peaks at BE of 530.1 and 531.3±0.2 eV. The first peak can be attributed to O^{2-} in TiO_2, and the second corresponds to OH groups. The large width of this peak (from 531 to 533 eV) results from the presence of not only OH groups but also NO_x and CO_x species [42–45]. From the spectra, one can also find that the surface of the samples contains more oxygen compared with the stoichiometric O/Ti ratio, confirming the presence of NO_x and CO_x.

The C 1s spectra of samples T-200 and T-400 are shown in Fig. 9. It is seen that there are certain differences in them. The content of carboxylate (COO) and carbonate (CO_3^-) groups on sample T-200 is about twice higher than that on sample T-400. If we exclude the C 1s line with 284.6±0.02 eV, which refers to carbon from oil vapors, then the carbon content corresponding to >C=O, CO_2^-, and CO_3^- species, is 7.5% on the surface of T-200 and 4.5% on T-400. These results agree with the IR data and show an excess carbon content on the surface of T-400 compared with nitrogen. In spectra of T-200, the weak peak corresponding to N 1 s with BE = 400 eV is observed for T-200 sample. There is no N 1s peak in sample T-400. The peak at BE = 400 eV is attributed to N-C bond, which is characteristic of different compound types [42, 43, 45]. In our experiments, XPS did not confirm the presence of TiC.

According to the XPS data, the main impurities on the surface of sample T-200 are not NO_x, but CO_2^- and CO_3^- species. Considering the IR data, this result suggests a predominantly bulk (inside the pores) rather than a surface arrangement of NO_x groups and surface arrangement of carbon-containing by-products of TiC oxidation in the $TiO_2 \cdot nH_2O$ structure.

The IR and XPS data suggest the availability of various products of titanium carbide oxidation with nitric acid (NO_x, CO_x), which modify the process of the TiO_2 microstructure formation. They are adsorbed on $TiO_2 \cdot nH_2O$, form a mesoporous structure, and prevent the coarsening of particles during heating, maintaining a high specific surface area of the samples. According to the experimental data, NO_x groups mainly influence the

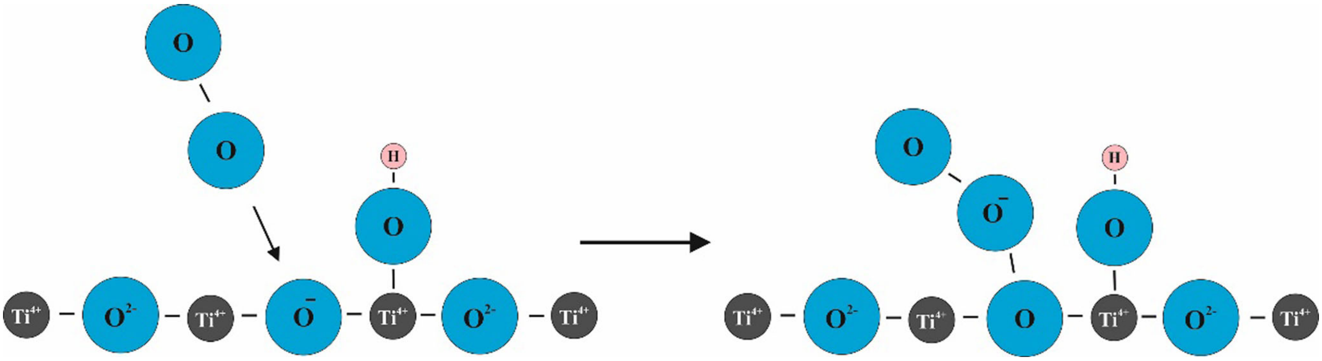

Fig. 8 Scheme of formation of paramagnetic center O^{3-} on titanium dioxide surface

Table 3 XPS Data for T-200 and T-400 Samples

Line	BE, eV	FWHM, eV	%	State, %*	FWHM, eV	%	State, %*
O 1s	530.1	1.4	63.5	O^{2-}, 70	1.2	62	O^{2-}, 84
	531.5	2.2	–	HO^-, 30	2.4	–	HO^-, 16
C 1s	284.8	1.7	12.5	C-C, C-H, 40	1.7	11	C-C, C-H, 59
	286.1	1.7	–	>C=O, 20	2.1	–	>C=O, 23
	288.9	1.4		COO^-, CO_3^-, 40	1.7		COO^-, CO_3^-, 18
Ti 2p$_{3/2}$	458.7	1.25	23.5	Ti^{4+} (TiO_2), 100	1.05	27	Ti^{4+} (TiO_2), 100
N 1s	400.2	–	0.5	NO_x	–		
	–	Sample T-200			Sample T-400		

*% each of the states of this element

formation of the bulk (porous and crystalline) structure of TiO_2, while carbonyl and carboxylate species remain on the TiO_2 surface.

Photocatalytic activity of rhodamine B

Figure 10 shows the change in the rhodamine B concentration in the solution over the TiO_2 suspension under the visible and UV light irradiation. Our samples are photoactive under the visible and UV irradiation, but their activity differs. Sample T-200 is the most active in dye photodecomposition under visible light irradiation (Fig. 10a). However, under the UV irradiation, sample T-400 possesses the highest activity (Fig. 10b). Sample T-200 is more photoactive than Degussa P25 in the visible region and sample T-400 in the UV region.

There is a correlation in the changes in the photoactivity of samples T-200 and T-400 in the dye bleaching reaction, when exposed to visible light and UV radiation.

The photoactivity decreases as follows:

$$T\text{-}200 > P25 > T\text{-}400 \ (visible\ light);$$
$$T\text{-}400 > P25 > T\text{-}200 \ (UV\ irradiation).$$

Considering the known ideas about the mechanisms of photocatalytic rhodamine B decomposition in the presence of a catalyst, one can explain the difference in the photoactive properties of the samples [46–48]. Typically, the decomposition of dyes on photocatalysts is characterized by a sensitization mechanism upon irradiation with visible light. Optical sensitization is based on a redox reaction between a photoexcited dye and TiO_2 [7, 8]. For this type of reaction to proceed effectively, an active TiO_2 surface is necessary, which, on the one hand, ensures the adsorption of dye molecules and, on the other hand, creates the energy levels necessary for the efficient electron transfer from the excited dye molecules to titanium dioxide [46]. Compared

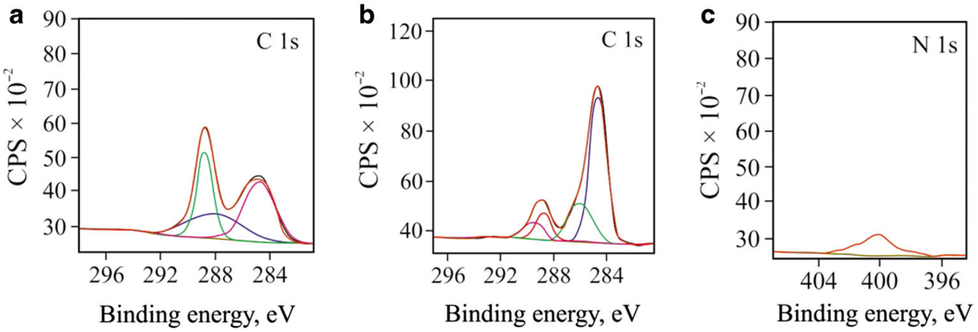

Fig. 9 XPS spectra of TiO_2 samples formed by oxidation of titanium carbide with nitric acid under different conditions: C 1s T-200 (**a**), C 1s T-400 (**b**), and N 1s T-200 (**c**)

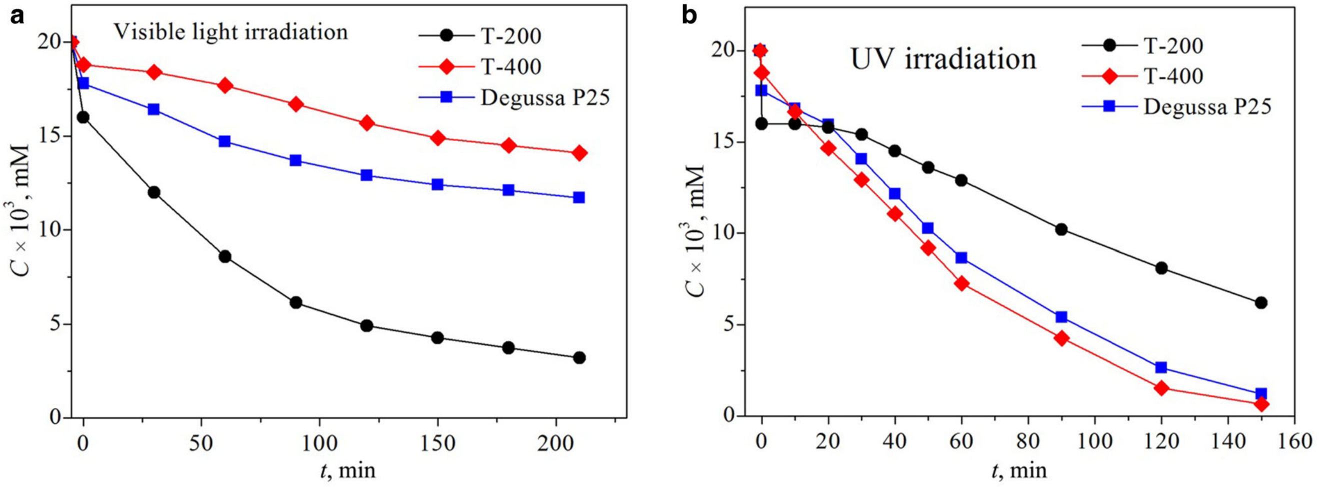

Fig. 10 Rhodamine B concentration in suspension of different TiO_2 samples (T-200, T-400, and Degussa P25) versus exposure to visible light (**a**) and ultraviolet (**b**) irradiation

with T-400 and Degusaa P25, sample T-200 possesses a better-developed surface and thus has an advantage in the dye molecule adsorption and activation, as well as dye oxidation according to this mechanism. The N- and C-containing impurities acting as sensitizing species on the sample surface can also increase the photocatalysis effectiveness under visible light irradiation [11–13, 49, 50]. An increased photodegradation of 4-chlorophenol was observed on the TiO_2 surface containing nitrogen [51] and carbon [52] under visible light irradiation (455 nm). The presence of a disordered phase in the T-200 sample, which has the rutile-type structure traces, would also increase the efficiency of photodecomposition by visible light [48, 53]. An active role of rutile clusters in the expanding photoactivity into the visible wavelength range was shown by Wang et al. [50]. The photoactivity of the mixed anatase + rutile system is higher than that of anatase.

The higher photoactivity of the T-400 sample in the UV region can be explained by the presence of O^- (O^{3-}) centers and their contribution to the oxidation reaction of dye molecules [37, 40]. Under UV irradiation, titanium dioxide is activated, which is accompanied by photogeneration of electron-hole pairs (e^-, h^+). The O^- (O^{3-}) center with electron-hole pairs results in a more efficient photoactivity of TiO_2. In addition, oxygen in TiO_2 suspensions plays a certain role in dye oxidation. The O^- hole centers can directly oxidize the adsorbed dye molecules or react with the surface hydroxyl groups to form OH radicals, strong oxidizers of organic molecules [46, 47].

The results of the study have shown that the approaches used to control the properties of titanium dioxide are promising, including the formation of a TiO_2 structure, limiting the recombination of photogenerated electron-hole pairs and the increase in the surface and its functionalization by a combination of various elements, groups, and structural defects. The materials greatly benefit from the ability to absorb both ultraviolet and visible light.

Conclusions

In this study, as a result of the oxidation of titanium carbide with nitric acid titanium dioxide a number of different samples have been formed with a mesoporous structure, a developed surface, and a particle size of less than 10 nm. The conditions of a subsequent heat treatment were found to affect the TiO_2 structural characteristics, the presence of impurities, and the photocatalytic activity in the dye decomposition reaction. The synthesized samples show high catalytic efficiency in the reaction of rhodamine B photodecomposition. It has been shown that compared with the well-known photocatalyst Degussa P25, the photocatalytic activity of the samples heat-treated at 200°C and 400 °C is improved when exposed to visible and UV radiation, respectively. The difference in the photocatalytic activity of the samples was explained, taking into account the specific features of their structure and their role in the processes of rhodamine B photodecomposition in solution over a TiO_2 suspension under visible light and UV radiation. The high photoactivity of TiO_2 sample (200°C) under exposure to visible light has been attributed to a large surface area, availability of CO_x and NO_x groups on the surface, and structure of the anatase phase with a trace of the rutile phase. Under exposure to UV radiation, TiO_2 sample (400°C) is characterized by high photoactivity due to a large surface area and oxygen structure defects (O^-). The proposed method for TiO_2 synthesis provides a simple tool for regulating the photocatalytic activity of titanium dioxide in the visible and UV regions by changing the heating temperature.

Funding This work was supported by the Belarusian Republican Foundation for Fundamental Research (Grant No. T23RNFM-35) and Russian Science Foundation (Grant No. 24-49-10012).

Author Contribution E. Ovodok: Conceptualization, Data curation, Visualization, Investigation. M. Ivanovskaya: Conceptualization, Supervision, Writing-Reviewing, and Editing, Methodology. S. Poznyak: Investigation, Supervision. K. Dzmitry: Writing-Original draft preparation. S. Zlotski: Investigation, Editing; V. Uglov: Supervision, Editing; Anton Seleznev: Investigation; A. Vereschaka: Editing, Methodology.

Data availability The datasets generated during and/or analyzed during the current study are available from the corresponding author on reasonable request.

Conflict of interest The authors have no competing interests to declare that are relevant to the content of this article.

References

1. Saeed, M., Muneer, M., Haq, A., Akram, N.: Photocatalysis: an effective tool for photodegradation of dyes—a review. Environ. Sci. Pollut. R. **29**, 293–311 (2022). https://doi.org/10.1007/s11356-021-16389-7
2. Gavrilenko, E.A., Goncharova, D.A., Lapin, I.N., Gerasimova, M.A., Svetlichnyi, V.A.: Photocatalytic activity of zinc oxide nanoparticles prepared by laser ablation in a decomposition reaction of rhodamine B. Russ. Phys. J. **63**, 1429–1437 (2020). https://doi.org/10.1007/s11182-020-02188-z
3. Das, R.S., Warkhade, S.K., Kumar, A., Wankhade, A.V.: Graphene oxide-based zirconium oxide nanocomposite for enhanced visible light-driven photocatalytic activity. Res. Chem. Intermed. **258**, 110043 (2019). https://doi.org/10.1007/s11164-018-3699-z
4. Bakina, O.V., Svarovskaya, N.V., Chzhou, V.R., Suliz, K.V.: Application of ultrasonic treatment for increasing the photochemical activity of tiO2-Ag Electroexplosive Bicomponent Nanoparticles. Russ. Phys. J. **65**, 1419–1423 (2023). https://doi.org/10.1007/s11182-023-02785-8
5. Maltanava, H., Poznyak, S., Ovodok, E.: Synthesis of znO mesoporous powders and their application in dye photodegradation. Mater Today: Proc. **5**, 17414–17421 (2018). https://doi.org/10.1016/j.matpr.2018.06.043
6. Chzhjou, V.R., Bakina, O.V., Svarovskaya, N.V., Khorobraya, E.G.: Modification of Polypropylene by Heterophase znO-Ag Nanoparticles. Russ. Phys. J. **67**, 1230–1236 (2024). https://doi.org/10.1007/s11182-024-03236-8
7. Mikhailova, S.L., Prikhodko, O.Y., Mukhametkarimov, Y.S.: Thermal stability of the structure and optical properties of nanostructured tiO2 films. Russ. Phys. J. **63**, 2045–2051 (2021). https://doi.org/10.1007/s11182-021-02272-y
8. Mikhailov, M.M., Vlasov, V.A.: A size effect in the optical properties of powdered tiO2. Russ Phys J **41**, 1222–1228 (1998). https://doi.org/10.1007/BF02514560
9. Divya, G., Jaishree, G., Sivarao, T., Lakshmi, K.D.: Microwave assisted sol-gel approach for Zr doped tiO 2 as a benign photocatalyst for bismark brown red dye pollutant. RSC Adv. **13**, 8692–8705 (2023). https://doi.org/10.1039/D3RA00328K
10. Keerthana, S.P., Yuvakkumar, R., Ravi, G.: Sr doped tiO_2 photocatalyst for the removal of Janus green B dye under visible light. RSC Adv. **13**, 18779–18787 (2023). https://doi.org/10.1039/D3RA00567D
11. Chung, K.H., Kim, B.J., Park, Y.K., Kim, S.C., Jung, S.C.: Photocatalytic properties of amorphous n-doped tiO2 photocatalyst under visible light irradiation. Catalysts **11**, 1010 (2021). https://doi.org/10.3390/catal11081010
12. Song, L., Jing, W., Chen, J.: High reusability and durability of carbon-doped tiO2/carbon nanofibrous film as visible-light-driven photocatalyst. J Mater Sci **54**, 3795–3804 (2019). https://doi.org/10.1007/s10853-018-3105-7
13. Jang, I., Leong, H.J., Noh, H.: et al.]: Preparation of N-functionalized TiO2 particles using one-step sol-gel method and their photocatalytic activity. J. Ind. Eng. Chem. **37**, 380–389 (2016). https://doi.org/10.1016/j.jiec.2016.04.002

14. Karuppasamy, P., Nisha, N.R.N., Pugazhendhi, A.: An investigation of transition metal doped tiO2 photocatalysts for the enhanced photocatalytic decoloration of methylene blue dye under visible light irradiation. J Environ Chem Eng. **9**, 105254 (2021). https://doi.org/10.1016/j.jece.2021.105254
15. Ovodok, E., Maltanava, H., Poznyak, S.: Sol-gel template synthesis of mesoporous carbon-doped tiO2 with photocatalytic activity under visible light. Mater. Today: Proc. **5**, 17422–17430 (2018). https://doi.org/10.1016/j.matpr.2018.06.044
16. Selvaraj, P., Roy, A., Ullah, H.: Soft-template synthesis of high surface area mesoporous titanium dioxide for dye-sensitized solar cells. Int J Energ Res. **43**, 523–534 (2019). https://doi.org/10.1002/er.4288
17. Zhou, W., Fu, H.: Mesoporous tiO$_2$: preparation, doping, and as a composite for photocatalysis. ChemCatChem **5**, 885–894 (2013). https://doi.org/10.1002/cctc.201200519
18. Shieh, D.L., Li, J.S., Shieh, M.J., Lin, J.L.: A novel approach to mesoporous anatase tiO2: oxidation of tiC by nitric acid. Micropor. Mesopor. Mat. **98**, 339–343 (2007). https://doi.org/10.1016/j.micromeso.2006.09.039
19. Ovodok, E., Maltanava, H., Poznyak, S.: Synthesis and characterization of efficient tiO2 mesoporous photocatalysts. Mater. Today: Proc. **4**, 11526–11533 (2017). https://doi.org/10.1016/j.matpr.2017.09.062
20. Ovodok, E., Maltanava, H., Poznyak, S.: Rhodamine-loaded tiO2 particles for detection of polymer coating UV degradation. Mater. Today: Proc. **20**, 320–328 (2020). https://doi.org/10.1016/j.matpr.2019.10.069
21. Ivanovskaya, M.: Ceramic and film metaloxide sensors obtained by sol-gel method: structural features and gas-sensitive properties. Electron Technol. **33**, 108–112 (2000)
22. Busca, G., Ramis, G., Amores, J.M.G.: FT Raman and FTIR studies of titanias and metatitanate powders. J. Chem. Soc. Faraday Trans. **90**, 3181–3190 (1994). https://doi.org/10.1039/FT9949003181
23. Nakamoto, K.: Infrared and Raman spectra of inorganic and coordination compounds (part A: theory and applications in inorganic chemistry), 6th edn. John Wiley & Sons Inc (2009). https://doi.org/10.1002/9780470405840
24. Addison, C.C., Amos, D.W., Sutton, D., Hoyle, W.H.H.: Infrared and Raman spectra of compounds containing bidentate nitrato-groups. J. Chem. Soc. A (1967). https://doi.org/10.1039/J19670000808
25. Davydov, A.: Molecular spectroscopy of oxide catalyst surfaces. Wiley, Chichester (2003). https://doi.org/10.1002/0470867981
26. Zhang, W.F., He, Y.L., Zhang, M.S.: Raman scattering study on anatase tiO2 nanocrystals. J. Phys. D: Appl. Phys. **33**, 912–916 (2000). https://doi.org/10.1088/0022-3727/33/8/305
27. Parker, J.C., Siegel, R.W.: Calibration of the Raman spectrum to the oxygen stoichiometry of nanophase tiO2. Appl. Phys. Lett. **57**, 943–945 (1990). https://doi.org/10.1063/1.104274
28. Hodkiewicz, J.: Characterizing carbon materials with Raman spectroscopy. Thermo Sci. Appl. Note (2010). https://www.semanticscholar.org/paper/Characterizing-Carbon-Materials-with-Raman-Hodkiewicz/bd887f696e5f7305f0e77d8d0f2aa7b35942cbbd
29. Atkins, P.W., Symons, M.C.: Structure of inorganic radicals; an application of electron spin resonance to the study of molecular structure. Elsevier, London (1967)
30. Carrington, A., McLachlan, A.D.: Introduction to magnetic resonance with applications to chemistry and chemical physics. New York, Evanston, London (1967)
31. Wertz, J.E., Bolton, J.R.: Electron spin resonance. New York (1972)
32. Valentin, C., Pacchioni, G., Selloni, A.: Characterization of paramagnetic species in N-doped tiO$_2$ powders by EPR spectroscopy and DFT calculations. J. Phys. Chem. B. **109**, 11414–11419 (2005). https://doi.org/10.1021/jp051756t
33. Mei, P., Henderson, M., Kassiba, A., Gibaud, A.: EPR study of nitrogen-doped mesoporous tiO$_2$ powders. J. Phys. Chem. Solids **71**, 1–6 (2010). https://doi.org/10.1016/j.jpcs.2009.08.002
34. Mizokawa, Y., Nakamura, S.: ESR study of the oxygen, hydrogen and nitrogen oxide on tin dioxide. Jpn. J. Appl. Phys. **2**, 253–256 (1974). https://doi.org/10.7567/JJAPS.2S2.253
35. Iyengar, R.D., Subba, R.V.V.: Electron spin resonance of nitrogen dioxide(NO2) adsorbed on zinc oxide. J. Amchem. Soc. **90**, 3267–3326 (1968). https://doi.org/10.1021/ja01014a068
36. Lunsford, J.H.: ESR of adsorbed oxygen species. Catal. Rev. **8**, 135–157 (1973). https://doi.org/10.1080/01614947408071859
37. Meriaudeau, P., Vedrine, J.C.: Electron paramagnetic resonance investigation of oxygen photoadsorption and its reactivity with carbon monoxide on titanium dioxide: the O 3-3 species. J. Chem. Soc. Faraday Trans. **72**, 472–480 (1976). https://doi.org/10.1039/F29767200472
38. Tench, A.J., Lawson, T.: The formation of O– and O3-adsorbed on an oxide surface. Chem Phys Lett **7**, 459–460 (1970). https://doi.org/10.1016/0009-2614(70)80335-9
39. Tench, A.J., Lawson, T., Kibblewhite, J.F.J.: Oxygen species adsorbed on oxides. Part 1.—formation and reactivity of (O–)s on mgO. J. Chem. Soc. Faraday Trans. **68**, 1169–1180 (1972). https://doi.org/10.1039/F19726801169
40. Tench, A.J.: Oxygen species adsorbed on oxides. Part 2.—formation of (O–3)s on mgO. J. Chem. Soc. Faraday Trans. **68**, 1181–1189 (1972). https://doi.org/10.1039/F19726801181
41. Mikheikin, I.D., Zhidomirov, G.M., Chuvylkin, N.D., Kazanskii, V.B.: Parameters of the ESR spectra and structure of O3-radicals. J. Struct. Chem. **15**, 678–681 (1974). https://doi.org/10.1007/BF00747267
42. Briggs, D., Seah, M.P.: Practical surface analysis by auger and X-ray photoelectron spectroscopy. John Wiley & Sons, New York (1983). https://doi.org/10.1002/sia.740060611

43. Restrepo Parra, E., Arango Arango, P.J., Benavides Palacio, V.J.: XPS structure analysis of tiN/tiC bilayers produced by pulsed vacuum arc discharge. Dyna **77**, 64–74 (2010)
44. Casanovas, J., Ricart, J.M., Rubio, J.: Origin of the large N 1s binding energy in X-ray photoelectron spectra of calcined carbonaceous materials. J. Am. Chem. Soc. **118**, 8071–8076 (1996). https://doi.org/10.1021/ja960338m
45. Arrigo, R., Havecker, M., Schlögl, R., Su, D.S.: Dynamic surface rearrangement and thermal stability of nitrogen functional groups on carbon nanotubes. Chem. Commun. (2008). https://doi.org/10.1039/B812769G
46. Linsebigler, A.L., Lu, G., Yates, J.T.: Photocatalysis on tiO2 surfaces: principles, mechanisms, and selected results. Chem. Rev. **95**, 735–758 (1995). https://doi.org/10.1021/cr00035a013
47. Carp, O., Huisman, C.L., Reller, A.: Photoinduced reactivity of titanium dioxide. Prog. Solid State Chem. **32**, 33–177 (2004). https://doi.org/10.1016/j.progsolidstchem.2004.08.001
48. Kumar, A., Khan, M., He, J., Lo, I.M.C.: Recent developments and challenges in practical application of visible-light-driven tiO2-based heterojunctions for PPCP degradation: a critical review. Water Res. **170**, 115356 (2020). https://doi.org/10.1016/j.watres.2019.115356
49. Li, Y., Hwang, D.S., Lee, N.H., Kim, S.J.: Synthesis and characterization of carbon-doped titania as an artificial solar light sensitive photocatalyst. Chem Phys Lett **404**, 25–29 (2005). https://doi.org/10.1016/j.cplett.2005.01.062
50. Wang, W., Ni, Y., Lu, C., Xu, Z.: Hydrogenation temperature related inner structures and visible-light-driven photocatalysis of N-F co-doped tiO2 nanosheets. Appl Surf Sci **290**, 125–130 (2014). https://doi.org/10.1016/j.apsusc.2013.11.013
51. Sakthivel, S., Kisch, H.: Photocatalytic and Photoelectrochemical properties of nitrogen-doped titanium dioxide. Chemphyschem **4**, 487–490 (2003). https://doi.org/10.1002/cphc.200200554
52. Lettmann, C., Hildenbrand, K., Kisch, H., Macyk, W., Maier, W.F.: Visible light photodegradation of 4-chlorophenol with a coke-containing titanium dioxide photocatalyst. Appl Catal B: Environ **32**, 215–227 (2001). https://doi.org/10.1016/S0926-3373(01)00141-2
53. Yi, J., Zhang, G., Wang, Y., Qian, W., Wang, X.: Recent advances in phase-engineered photocatalysts: Classification and diversified applications. Mater. **16**, 3980 (2023). https://doi.org/10.3390/ma16113980

Authors and Affiliations

E. A. Ovodok[1] · M. I. Ivanovskaya[1] · S. K. Poznyak[1] · D. A. Kotsikau[2] · S. V. Zlotski[2] · V. V. Uglov[2] · A. E. Seleznev[3] · A. A. Vereschaka[4]

✉ E. A. Ovodok
ovodok@bsu.by

M. I. Ivanovskaya
Ivanovskaya@bsu.by

S. K. Poznyak
spoznyak@gmail.com

D. A. Kotsikau
kotsikau@yandex.by

S. V. Zlotski
Zlotski@bsu.by

V. V. Uglov
Uglov@bsu.by

A. E. Seleznev
a.seleznev@stankin.ru

A. A. Vereschaka
dr.a.veres@yandex.ru

[1] Research Institute for Physical Chemical Problems of the Belarusian State University, Minsk, Belarus

[2] Belarusian State University, Minsk, Belarus

[3] Moscow State University of Technology, STANKIN, Moscow, Russian Federation

[4] Institute of Design and Technological Informatics of the Russian Academy of Sciences (IDTI RAS), Moscow, Russian Federation